

Structure and vibrational properties of sodium silicate glass surfaces

Cite as: J. Chem. Phys. **153**, 124503 (2020); <https://doi.org/10.1063/5.0019514>

Submitted: 23 June 2020 . Accepted: 30 August 2020 . Published Online: 23 September 2020

Zhen Zhang , Simona Ispas , and Walter Kob 



View Online



Export Citation



CrossMark

Lock-in Amplifiers
up to 600 MHz



Structure and vibrational properties of sodium silicate glass surfaces

Cite as: J. Chem. Phys. 153, 124503 (2020); doi: 10.1063/5.0019514

Submitted: 23 June 2020 • Accepted: 30 August 2020 •

Published Online: 23 September 2020



View Online



Export Citation



CrossMark

Zhen Zhang,  Simona Ispas,  and Walter Kob^{a)} 

AFFILIATIONS

Laboratoire Charles Coulomb, University of Montpellier, CNRS, F-34095 Montpellier, France

^{a)} Author to whom correspondence should be addressed: walter.kob@umontpellier.fr

ABSTRACT

Using molecular dynamics simulations, we investigate how the structural and vibrational properties of the surfaces of sodo-silicate glasses depend on the sodium content as well as the nature of the surface. Two types of glass surfaces are considered: A melt-formed surface (MS) in which a liquid with a free surface has been cooled down into the glass phase and a fracture surface (FS) obtained by tensile loading of a glass sample. We find that the MS is more abundant in Na and non-bridging oxygen atoms than the FS and the bulk glass, whereas the FS has higher concentration of structural defects such as two-membered rings and under-coordinated Si than the MS. We associate these structural differences to the production histories of the glasses and the mobility of the Na ions. It is also found that for Na-poor systems, the fluctuations in composition and local atomic charge density decay with a power-law as a function of distance from the surface, while Na-rich systems show an exponential decay with a typical decay length of ≈ 2.3 Å. The vibrational density of states shows that the presence of the surfaces leads to a decrease in the characteristic frequencies in the system. The two-membered rings give rise to a pronounced band at ≈ 880 cm⁻¹, which is in good agreement with experimental observations.

Published under license by AIP Publishing. <https://doi.org/10.1063/5.0019514>

I. INTRODUCTION

Silicate glasses are not only ubiquitous in many technical applications and in our daily life but also in the focus of many scientific studies.^{1–3} For many practical applications of glasses, such as displays of electronic devices and biomedical containers, the properties of the glass surface are highly important since the coating and structuring of the surface allows us to devise novel functional materials.^{4–9} A further motivation to study the surfaces of glasses is that such investigation allows us to obtain a better understanding of the failure mechanisms of bulk glasses, since very often fracture starts at the surface defects of the sample.^{10,11} Analyzing the post-mortem fracture surface (FS) of broken glass allows thus to gain insight on the origin of the failure and the way the fracture front propagates, knowledge that is valuable for obtaining a deeper understanding of fracture of amorphous materials.^{12–21}

One of the primary goals of surface characterization is to determine the composition and microstructure of the sample. In experiments, this can be done, e.g., by spectroscopic techniques such as low-energy ion scattering (LEIS) spectroscopy, X-ray photoelectron

spectroscopy (XPS), or atomic force microscopy (AFM).^{22–29} Ion scattering spectroscopy study have revealed that the fracture surface of silica glass shows an abundance of oxygen atoms and that the fracture surface of potassium trisilicate glass has a potassium concentration that is higher than the one of the bulk composition,²² a result which was attributed to the charge shielding on the surface. More recent studies using LEIS investigated the melt-formed and fracture surfaces of binary silicate glasses.^{23,24} It was shown that, when compared with the bulk composition, the melt-formed surfaces (MS) are usually depleted of the modifier atoms (i.e., Na), which was hypothesized to be a consequence of surface evaporation while the sample was still in the liquid state. In contrast to this, the fracture surfaces were found to be enriched in alkali species, while depleted of divalent barium (which was attributed to the immobility of the Ba²⁺ cations). The authors of that study also investigated the depth profiles of elemental concentration and were able to detect the presence of concentration gradient normal to the glass surfaces.²⁴ Also, spectroscopic studies are useful to determine structural features of the glass surface. For example, infrared measurements allowed to identify an interesting structural motif on the

surfaces of silicate glasses, namely two-membered (2M) rings,^{30–36} i.e., closed loops of two oxygen and two silicon atoms. Such metastable rings, which are absent in the bulk, are of particular interest since they form reactive sites on the surface.^{31–35,37} Also, the AFM has proven to be a valuable tool for direct imaging the structural features on glass surfaces with atomic resolution, allowing to access structural information such as interatomic distances and grouping of atoms.^{26–29}

To summarize, these experimental studies have given clear evidence that the composition and structure of glass surfaces are different from the ones of the bulk. In addition, the surface composition and structure were also found to depend strongly on the processing history. However, it should be noted that these spectroscopic data are essentially semi-quantitative, and the results depend also on the environment under which the measurements were performed. As a consequence, we are at present still lacking a good understanding about the composition and structure of the glass surfaces and how these properties depend on the system considered.^{38,39}

In addition to experimental studies, computer simulations have also been used to probe the microscopic properties of glass surfaces, particularly for the case of silica.^{37,40–44} To characterize the simulated surface, one often defines a surface layer, the thickness of which is usually determined from properties such as the density profile in the orthogonal direction with respect to the surface, see, for example, in Ref. 42. These simulation studies have revealed the presence of structural units such as nonbridging oxygen, 2M rings, and undercoordinated Si on the glass surfaces in qualitative agreement with the experimental findings. However, the vibrational spectrum and other properties that require a reliable interaction potential are rarely reported,^{42,45} despite their relevance for experiments. In addition, at present, it remains poorly understood how the change in glass composition, e.g., different concentration of alkali oxides, affects the surface structure and other related properties.^{38,39}

The objective of the present work is to investigate how the properties (structure, composition, vibrational spectra, ...) of the glass surface depend on the production history and the composition. To this end, we perform large scale atomistic simulations to produce sodium silicate glasses with varied content of Na₂O and compare the characteristics of the melt-formed surface (MS) with the ones of the fracture surface (FS) of the glasses.

The rest of this paper is organized as follows: In Sec. II, we give the details of the simulations and the way we have defined and analyzed the surface. Section III is devoted to the obtained results and related discussion, while in Sec. IV, we summarize and draw conclusions of this work.

II. METHODOLOGY

A. Simulation details

We carried out molecular dynamics simulations to probe the surface properties of SiO₂ and Na₂O-*x*SiO₂ (NS_{*x*}) glasses. We choose the compositions with *x* = 3, 4, 5, 7, 10, and 20, and together with SiO₂, these compositions correspond to a Na₂O concentration that varies from 0 mol. % to 25 mol. %. To start the simulations, we randomly placed around 2 300 000 atoms in the simulation box, which has a fixed volume corresponding to the experimental value of

glass density at room temperature.^{46,47} [The glass density increases from 2.20 g/cm³ for silica to 2.43 g/cm³ for NS3 (25% Na₂O).] The dimensions of the boxes were roughly 20 × 30 × 50 nm³. Such large samples (surface areas are 600 nm² and 1000 nm² for the melt and fracture surfaces, respectively) are necessary to obtain results with high accuracy, in particular, for the case of the fracture surfaces. These samples, with periodic boundary conditions applied, were first melted and equilibrated at 6000 K for 80 ps in the canonical ensemble (*NVT*) and then cooled and equilibrated at a lower temperature *T*₁ (still in liquid state) for another 160 ps, see Fig. 1(d). The temperature *T*₁ ranges from 3000 K for SiO₂ to 2000 K for NS3 (25 mol. % Na₂O), and its *x*-dependence reflects the fact that the viscosity of NS_{*x*} depends strongly on *x*. Subsequently, we cut the sample orthogonal to the *z*-axis and added an empty space, thus creating two free surfaces, i.e., the sample had the geometry of a sandwich, see Fig. 1(a). Periodic boundary conditions were maintained in all three directions. In order to ensure that the two free surfaces do not interact with each other, the thickness of the vacuum layer varied from 6 nm for silica to 14 nm for NS3. The samples with free surfaces were then equilibrated at *T*₁ for 1.6 ns, a time span that is sufficiently long to allow the reconstruction of the surfaces and the equilibration of the interior of the samples. (The averaged displacement of Si in silica and NS3 is larger than 40 Å and 6.2 Å, respectively.) Following this equilibration, the liquid samples were cooled via a two-stage quenching: A cooling rate of $\gamma_1 = 0.125$ K/ps was used to quench the sample from *T*₁ to a temperature *T*₂ and a faster cooling rate $\gamma_2 = 0.375$ K/ps to cool it from *T*₂ to 300 K, see Fig. 1(b). Finally, the samples were annealed at 300 K for 800 ps. The temperature *T*₂ at which the cooling rate changes was chosen to be at least 200 K below the simulation glass transition temperature *T*_g, see Fig. 1(d). At *T*₂, we also switched the simulation ensemble from *NVT* to *NPT* (at zero pressure).

The described simulation protocol has the advantages that (1) the fast cooling below *T*_g saves computer time while retaining statistically the same structure as slow cooling and (2) the *NVT* simulation in the high $-T$ range helps to retain a regular shape of the sample. Below *T*_g, the sample has more or less a regular shape and switching to the *NPT* ensemble allows us to release internal stresses and facilitate local structural rearrangements. In the following, we will refer to the two surfaces of the sandwich glass samples as the melt-formed surfaces (MS).

The sandwich glass samples were subsequently notched on one surface and then subjected to a uniaxial strain in the *y*-direction until complete fracture occurred, creating thus two fracture surfaces, see Fig. 1(c). The cross section of the introduced triangular notch had a width and height of 3 nm and 2 nm, respectively (more details in Ref. 50), and the strain rate was chosen to be 0.5 ns⁻¹, a value that is small enough to obtain the results that do not depend in a significant manner on the rate.^{50,51} The fracture simulations were done in the *NPT* ensemble at zero pressure, i.e., the pressures in the directions orthogonal to the loading direction are set to zero, allowing the sample to relax in the *x* and *z* directions. (This constant pressure ensemble is more similar to real experiments than the constant volume ensemble since the latter induces artifact brittle fracture behavior of the sample under tension.^{51,52}) We note that the current simulation setup mimics the plane stress condition, i.e., a thin slab in the *x*-*y* plane with the stress component $\sigma_{\alpha z} = 0$, for $\alpha = x, y, z$.

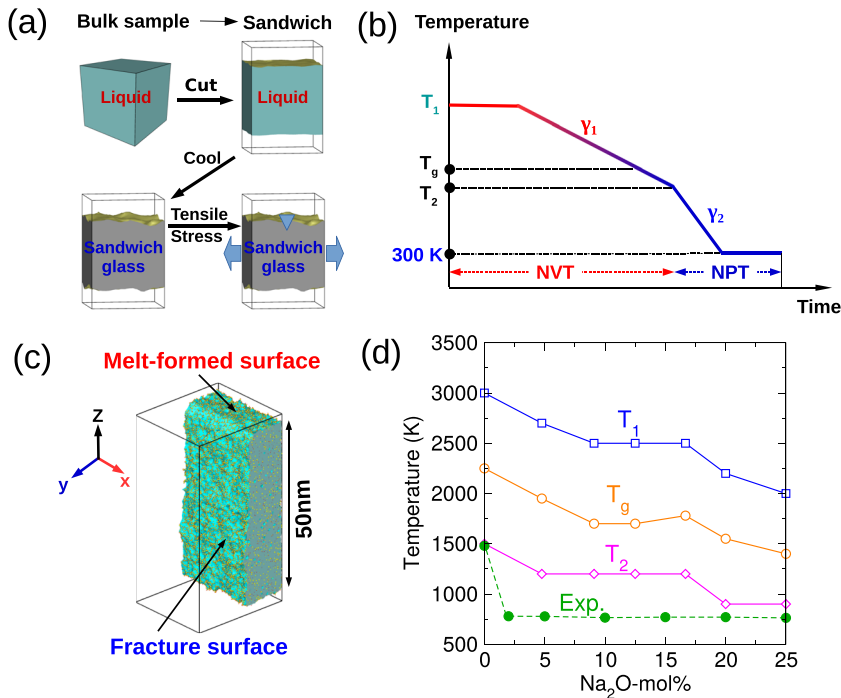


FIG. 1. Schematic drawing of the simulation procedures. (a) Preparation of the sandwich glass sample. (b) Temperature profiles of the melt-quench procedure. See the text for the definitions of the various T_s . (c) A silica glass after fracture. The melt-formed and fracture surfaces are indicated by the arrows. (d) Compositional dependence of various characteristic temperatures in the simulations. The glass transition temperature T_g was determined as the T at which the extrapolated total energy vs temperature curves of the liquid and glass cross. The uncertainty of the estimated T_g is about ± 50 K. Also included in the graph are the experimental T_g (filled circles) measured by using the calorimetric method for $\text{Na}_2\text{O}-x\text{SiO}_2$ ⁴⁸ and for SiO_2 ⁴⁹ ($\Delta T_g = \pm 3$ °C).

For the simulations, we used a pairwise effective potential named SHIK, which has been demonstrated to give a reliable description of the structural and mechanical properties of sodium silicate glasses.^{51,53} Its functional form is given by

$$V(r_{ij}) = \frac{q_i q_j e^2}{4\pi\epsilon_0 r_{ij}} + A_{ij} e^{-r_{ij}/B_{ij}} - \frac{C_{ij}}{r_{ij}^6}, \quad (1)$$

where r_{ij} is the distance between two atoms of species i and j . This potential uses partial charges q_i for different atomic species: The charges for Si and Na are, respectively, fixed to $1.7755e$ and $0.5497e$, while the charge of O depends on the composition and is given by ensuring charge neutrality of the sample, i.e.,

$$q_{\text{O}} = \frac{(1-y)q_{\text{Si}} + 2yq_{\text{Na}}}{2-y}, \quad (2)$$

where y is the molar concentration of Na_2O , i.e., $y = (1+x)^{-1}$. The other parameters of the potential, A_{ij} , B_{ij} and C_{ij} , occurring in Eq. (1) are given in Ref. 51. It is also worth mentioning that these parameters of the SHIK potential were optimized by using bulk properties obtained from experiments and *ab initio* calculations.⁵³ To the best of our knowledge, it is the first time that this potential is used to study dry surfaces of glasses.

Temperature and pressure were controlled using a Nosé-Hoover thermostat and barostat.⁵⁴⁻⁵⁶ All simulations were carried out using the Large-scale Atomic/Molecular Massively Parallel Simulator software (LAMMPS)⁵⁷ with a time step of 1.6 fs. The results presented in the following section correspond to one melt-quench sample for each composition. However, we emphasize that the system sizes considered in this study are sufficiently large to make

sample-to-sample fluctuations negligible. For the MS, the results for the two surfaces on the top and bottom sides of the glass sample were averaged. For the FS, four surfaces, resulting from two independent fractures (by changing the location of the notch), were averaged. For each sample, the number of surface atoms was typically around 11 000 for the MS and 18 000 for the FS.

B. Construction of the geometric surface

In atomistic simulations, constructing the surface of a solid corresponds to define the geometric boundary of a set of points in space (the atoms), which allows us to divide volume into solid and empty regions. Figure 2 schematically shows the procedure for constructing the geometric surfaces of the glass samples. To start, we have used the alpha-shape method proposed by Edelsbrunner and Mücke⁵⁸ to construct a surface mesh. For the case of two dimensions, this method relies on the Delaunay triangulation (DT) of the input point set, see Fig. 2(a). For a given set \mathbf{P} of discrete points, the triangulation $\text{DT}(\mathbf{P})$ is done in such a way that no point in \mathbf{P} is inside the circumcircle of any triangle in $\text{DT}(\mathbf{P})$. For the three-dimensional case, the circumcircle extends naturally to a circumscribed sphere, which touches each of the tetrahedron's vertices (Delaunay tetrahedrization). All tessellation elements are then tested by comparing their circumspheres to a reference probe sphere, which has a radius of R_α . The elements (with circumsphere radius R) that satisfy $R < R_\alpha$ are classified as solid, and the union of all solid Delaunay elements defines the geometric shape of the atomistic solid. The mesh points that define this geometric surface are the atoms on the outermost surface layer, Fig. 2(c), i.e., this surface layer has, by construction, a thickness of zero, and R_α is only a length scale used to construct it.

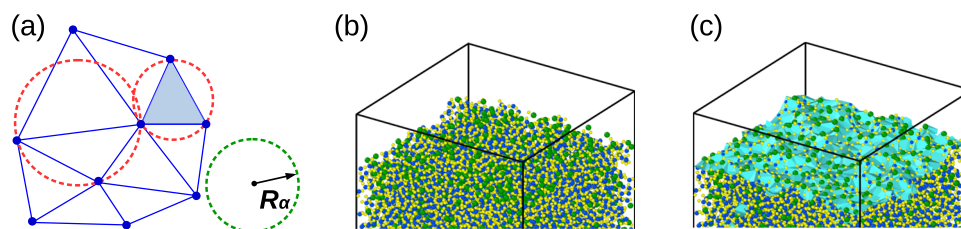


FIG. 2. Schematics of the procedure for constructing the geometric surface. (a) Delaunay triangulation of a set of points. The reference probe sphere (with radius R_α) is also shown. The triangular element whose circumsphere is smaller than R_α is classified as solid (e.g., the shaded triangle). (b) Atomic model of the sandwich sample at 300 K. (c) Constructed polyhedral surface mesh. The shown sample is NS10, and the constructed surface is a melt-formed surface.

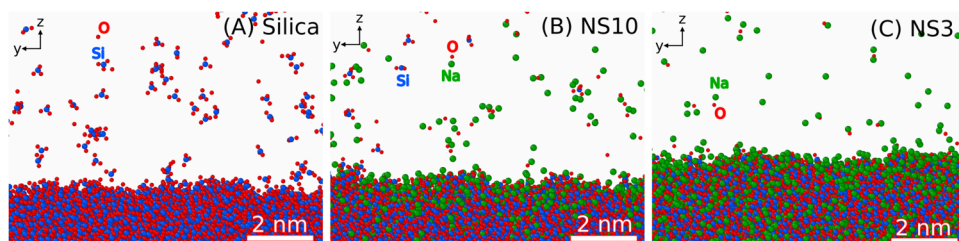


FIG. 3. Snapshots of the atomic structure near the surfaces of the liquid samples. (a) Silica at 3000 K, (b) NS10 at 2500 K, and (c) NS3 at 2000 K.

It is also important to mention that the probe sphere radius R_α is the length scale, which determines how many details and small features of the solid's geometric shape are resolved. Usually, the value of R_α should be chosen to represent the average spacing between the basic structural units in a material.⁵⁹ For the investigated silicate glasses, we have chosen $R_\alpha = 3.2 \text{ \AA}$, which corresponds approximately to the nearest neighbor distance between two $[\text{SiO}_4]$ tetrahedra. By visual inspection of the constructed surface, we find that the chosen R_α allows us to resolve fine surface features while avoiding artificial holes in the constructed surfaces. We note, however, that a small change in R_α (e.g., $\pm 0.5 \text{ \AA}$) will not significantly alter the results presented in the following (more detailed tests can be found in Ref. 50). Visualization of the atomic models and the surface mesh were realized by using the OVITO software.⁶⁰ Finally, we mention that the procedure for constructing the FS is the same as the one for the MS. However, for the FS, we have eliminated the atoms that were closer than $\approx 5 \text{ nm}$ to the top/bottom MS in order to avoid the influence of these surfaces onto the properties of the FS.

III. RESULTS AND DISCUSSION

A. Composition of the vapor during the melt-quench process

Before we discuss the properties of the glass surfaces, it is instructive to look at the simulation samples at high temperatures, notably at the vapor phase, since this allows us to understand better how the melt surfaces are formed.

Figure 3 shows snapshots of a part of the samples close to one of the surfaces at the temperature T_1 , i.e., when the samples are still in the liquid state, see Fig. 1(d). For silica, panel (a), one recognizes that most Si atoms in the vapor are surrounded by three O atoms,

and therefore, one can expect that in the vapor, the ratio between the fractions of O and Si is around 3. (Note that one also finds free oxygen atoms.) With the addition of Na, NS10 panel (b), the concentration of Si atoms in the vapor phase decreases quickly since they are replaced to a large extent by the Na atoms, which are more volatile and still allow for (partial) charge compensation. The trend of Si being replaced by Na continues if the Na content is increased further, NS3 panel (c). One sees that for NS3, there are basically no Si atoms in the vapor phase. This result agrees with the experimental finding that O and alkali (Na and K) atoms will evaporate from the surfaces of alkali trisilicate glass at elevated temperatures, while Si atoms remain at the surface and in the bulk.⁶¹ It is worth to mention that since the temperature considered for the three snapshots are not the same, the reduction of Si content in the vapor may partially be attributed to the decreased temperature for the samples containing Na (see below).

In order to get a more quantitative understanding of these observations, we show in Fig. 4 the number density of atoms, ρ_{num} , (upper panels) and the fractions of various atomic species (lower panels) in the vapor phase as a function of time during the equilibration (first 2 ns) and during the quench of the system. (These quantities were determined by averaging the density/composition over a slab of width 4 nm and orthogonal to the z direction in the central part of the void.) For silica, panel (a), one sees that ρ_{num} increases while the system is at 3000 K, indicating that more and more atoms in the near-surface region evaporate to the vacuum, demonstrating that the sample is above the boiling point. Once the temperature is lowered, ρ_{num} quickly decreases, and for T below 1400 K, only very few atoms remain in the gas phase. Interestingly, one finds that the relative concentrations of O and Si in the vapor are independent of temperature and that the ratio between O and Si is around 3.2, panel (b). This result indicates that at these temperatures, each Si atom

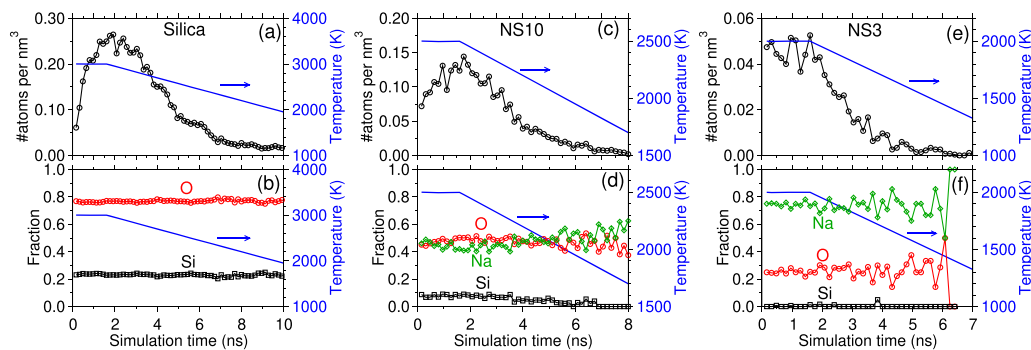


FIG. 4. [Panels (a), (c), and (e)] Number density of atoms in the vapor of the samples during the melt-quench process. [Panels (b), (d), and (f)] Fractions of different atomic species in the vapor. From left to right, the compositions are silica, NS10 and NS3, respectively.

moving in and out from the surface is typically associated with three O atoms, in agreement with the snapshot in Fig. 3(a). Note that it is not obvious why the Si/O ratio takes this value since the formation of the SiO_3 molecules is a compromise between charge neutrality, corresponding to SiO_2 , and the attractive part of the short range potential in the Si–O interaction.

With increasing Na_2O content, panels (c) and (e), the density of atoms in the vapor decreases considerably relative to the silica one. This result is on one hand due to the reduced temperature of equilibration [Fig. 1(d)] and on the other hand because of the increased volume of the vacuum layer. Regarding the composition of the vapor, one finds that for NS10, panel (d), the fraction of Si is around 10% during the equilibration and then decreases with lowering T , while the Na fraction is around 50%, and this number increases slightly as the temperature decreases. For NS3, panel (f), the enrichment of Na in the vapor is even more pronounced than in NS10, reaching a concentration of around 75% (compared to the nominal fraction of $\text{Na} = 16.7\%$ for NS3), while the concentration of Si in the vapor becomes negligible, a result that is consistent with the observation from the snapshot in Fig. 3(c). Interestingly, one finds that the relative concentration between Na and O is around 3, independent of temperature.

Finally, we note that if one multiplies the concentration of the various atoms with their respective charges, one finds that the total charge of the vapor phase is negative for silica and NS10, panels (b) and (d), while it is positive for NS3, panel (f). Consequently, the condensed phases are also not charge neutral. As we will see below, this charge imbalance of the two phases has consequences in the surface properties.

B. Monolayer surface composition and structure

Having understood the composition of the vapor phase at elevated temperatures, we now focus on the surface properties at 300 K. To start, we characterize the local structure of the surfaces by the distributions of interatomic distances and bond angles and compare these distributions with the ones of the bulk glass. These bulk data are obtained by considering only the atoms in a cube with a side length of 120 Å in the geometric center of the sandwich glass, i.e., these atoms have a distance of at least 190 Å from any free surface

and thus can be expected to reflect the bulk behavior of the glass sample.

Figure 5 shows the distributions of nearest neighbor distances for various pairs. For clarity, we show only the results for three representative compositions, namely, silica, NS10 (Na-poor) and NS3 (Na-rich). For Si–O, panels [(a)–(c)], one recognizes that the distributions for the surfaces and the bulk are very similar to each other, indicating that the presence of the surface does not modify significantly the bonding distance. Nevertheless, one sees that the distribution for the bulk is narrower than the one of the free surfaces and that the FS has a distribution that is somewhat broader than the one of the MS. The latter result is reasonable since the FS has more structural defects (see below). For the Si–Si distances, panels [(d)–(f)], we find for the surfaces a pronounced peak at ≈ 2.4 Å, a feature that is completely absent in the distribution for the bulk sample. (Note that the MS curves for NS10 and NS3 are not shown since they are too noisy as only a small number of Si atoms is found on the surface.) This peak arises from the two-membered (2M) rings in which two edge-sharing Si atoms (esSi) are connected by two edge-sharing bridging O atoms (esBO), as already documented in previous studies.^{30–35,42,43,45,62,63}

Figures 5(a)–5(c) show that the PDFs for the Si–O distances of the FS are wider than the ones of the bulk and that in addition they show a weak splitting. In order to identify the origin of these two features, we have decomposed the distributions into various contributions, and in Fig. 6, we show the result of this decomposition for the cases of the FS of silica and NS3. One recognizes that the distance between Si and non-bridging oxygen (NBO) is somewhat smaller than the one for Si and bridging oxygen (BO), leading to a slight broadening of the peak, panels (a) and (d). In addition, the distance between a Si^3 (a silicon atom bonded to three oxygen atoms) and an oxygen is smaller than the one between Si^4 and oxygen, panel (b), contributing to the widening of the peak at small r . Finally, we find that the splitting of the Si–O peak close to the maximum is related to the fact that the Si–O distance in a 2M ring is slightly larger than the one of a corner shared tetrahedron, panels (c) and (f).

Figure 7(a) shows the concentrations of Si and esSi as a function of Na_2O content for the surfaces. As a reference, we have included in the graph also the concentration of Si in the bulk state (black dashed line), which decreases linearly with the Na concentration. The graph

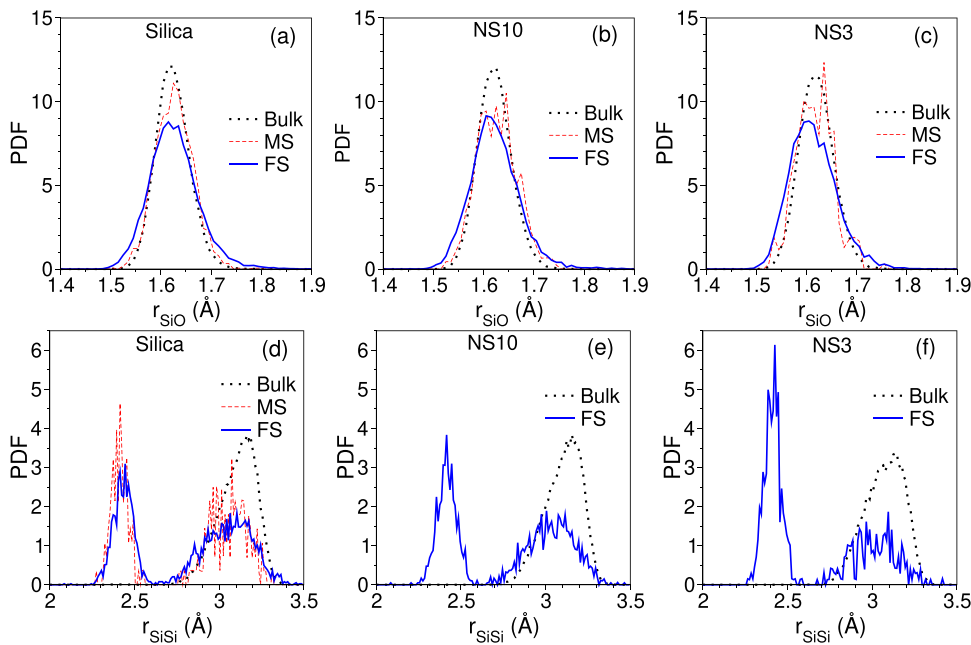


FIG. 5. Probability distribution function (PDF) of the nearest neighbor distance. Panels (a)–(c) are for Si–O pairs, and panels (d)–(f) for Si–Si pairs. From left to right, the compositions are silica, NS10, and NS3, respectively.

demonstrates that, due to the enrichment of O and Na atoms on the surfaces, the surface concentration of Si is considerably lower than the bulk one. Furthermore, one sees that for the FS, the concentration of esSi is considerably higher than the one of the MS, i.e., the former surface is more abundant in 2M-rings than the MS, a

trend that can be understood directly from the production process of the two types of surfaces. For the FS, both the Si and esSi fractions decrease in a linear manner with the Na_2O content, showing that on the surface, the Si atoms are readily replaced by Na atoms. The graph also demonstrates that the Si concentration in the MS depends very

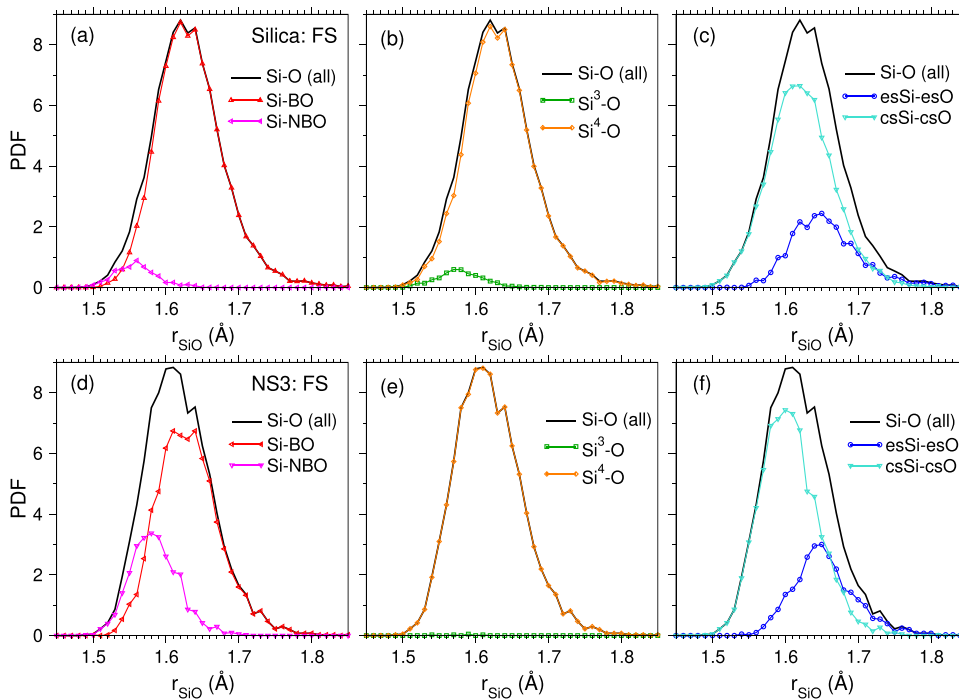


FIG. 6. Decomposition of the SiO PDFs for the FS of silica (top row) and NS3 (bottom row). Panels (a) and (d) show decomposition with respect to oxygen species, bridging (BO) and non-bridging (NBO). Panels (b) and (e) show decomposition with respect to silicon atoms that are three- and four-fold coordinated. Panels (c) and (f) show decomposition with respect to atoms that are in edge-sharing and corner-sharing tetrahedra.

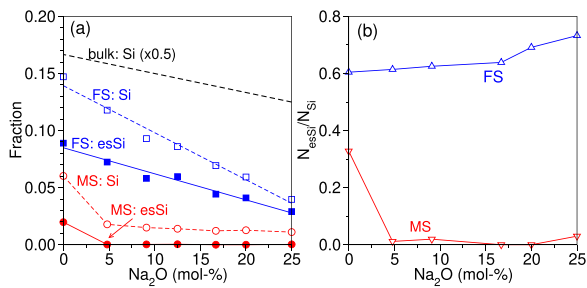


FIG. 7. (a) Fraction of Si and esSi on the surfaces. The bulk data are multiplied by 0.5 to allow better comparison with the surface data. The blue solid and dashed lines are linear fits to the FS data. (b) The ratio between the fractions of esSi and Si on the surfaces.

weakly on the Na₂O content. The only exceptions are the Na-poor compositions in that one observes a drastic decrease in the concentration of Si at the surface if one goes from pure silica to a glass with 5% Na₂O. This result is directly related to the fact that the MS is created in the liquid state, which allows more Na to diffuse to the surface and thus to reorganize the surface structure by reducing the concentration of Si atoms and hence the local stress.

The ratio between the fractions of esSi and Si on the two types of surface are plotted in Fig. 7(b). One recognizes that for the FS, over 60% of Si atoms are in the 2M-ring structures and that this ratio slightly increases with increasing Na₂O content. [Note that the observation that more than 60% of the Si atoms are in 2M rings does not imply that these rings are frequent since the overall concentration of Si at the surface is low, see Fig. 7(a).] The MS, by contrast, only has a negligible fraction of esSi on the surface, except for silica for which around 30% of Si are esSi. We mention here that the FS was generated by fast cracking ($\approx 10^3$ m/s⁵⁰) at room temperature, and therefore, one can expect that only very little reconstruction of the fracture surface has occurred after the crack has passed.

As discussed above, the FS has quite a few 2M rings, structures that are basically absent in the bulk. We thus conclude that these small rings are created during the fracture process since the passing of the crack front makes that many bonds are broken. The so created dangling bonds are energetically highly unstable and hence will try to reform as quickly as possible. This process can be expected to lead to many short loops, and hence 2M rings, since the formation of larger rings, although energetically more favorable than short rings, takes much more time since it involves a cooperative motion of several atoms. For the case of the MS, the system has more time to form these large rings, and hence, in this case, the 2M rings are basically absent.

In Fig. 8, we show the distributions of the nearest neighbor distances for the Na–O (r_{NaO}) and Na–Na (r_{NaNa}) pairs. [Note that we are plotting here the PDF of the nearest neighbor distances between atoms in the surface layer, which is different from the partial radial distribution functions $g_{\text{NaO}}(r)$ [2]. The latter is the spherical average of the PDF divided by $4\pi r^2$.] For Na–O, panels (a) and (b), one recognizes that the two curves for the surfaces are nearly identical, indicating that the relative arrangement of surface O and Na is independent of the nature of the surface, despite the fact that for the two

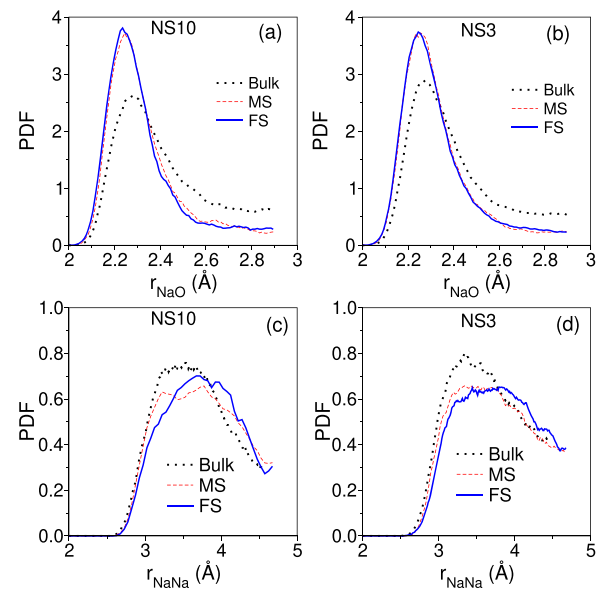


FIG. 8. Probability distribution function (PDF) of the nearest neighbor distance. Panels (a) and (b) are for Na–O pairs, and panels (c) and (d) for Na–Na pairs. Left and right columns are for NS10 and NS3, respectively.

surfaces, the Na concentration is very different (see Fig. 10 below). Furthermore, we note that the distributions of the r_{NaO} distances for the two surfaces are narrower and peak at a smaller distance than the one of the bulk. This finding indicates that the most probable Na–O bond length on the surfaces is slightly smaller than the typical value found in the bulk. The rationale is that on the surfaces, the atoms have less constraints, and thus, the Na and O atoms are more likely to form bonds that are energetically more favorable.

For the Na–Na distance, panels (c) and (d), one notices that also here the distributions for the two surfaces are very similar but that now these distributions are slightly broader than the one for the bulk. This observation might indicate that on the surface, the Na arrangement (with respect to the Si–O network) is more disordered than in the bulk, but it might also be related to the increased local concentration of Na atoms.

Figure 9 shows the bond angle distributions for O–Si–O and Si–O–Si linkages. (Links are defined via the first minimum in the corresponding radial distribution function, i.e., 2.0 Å.) For O–Si–O, panels [(a)–(c)], one sees that the curves for the surfaces have a peak at the intra-tetrahedral angle 109°, which is broader than the one of the bulk. For the FS, this peak is the widest, showing that the structure of this surface has the strongest disorder. A further feature to be noticed is the peak at $\approx 85^\circ$, notably for the FS curves. This peak is another signature of the 2M-rings, in addition to the distance $r_{\text{SiSi}} = 2.4$ Å, Figs. 5(d)–5(f). The presence of these 2M-rings can also be seen in the distribution of the (inter-tetrahedral) Si–O–Si angle, Figs. 9(d)–9(f), in that one finds a marked peak at $\approx 95^\circ$. In fact, this peak is the dominant one for the FS, while it is completely absent in the bulk sample, showing that the 2M-rings are very important structural motifs for the FS. (Note that for NS10

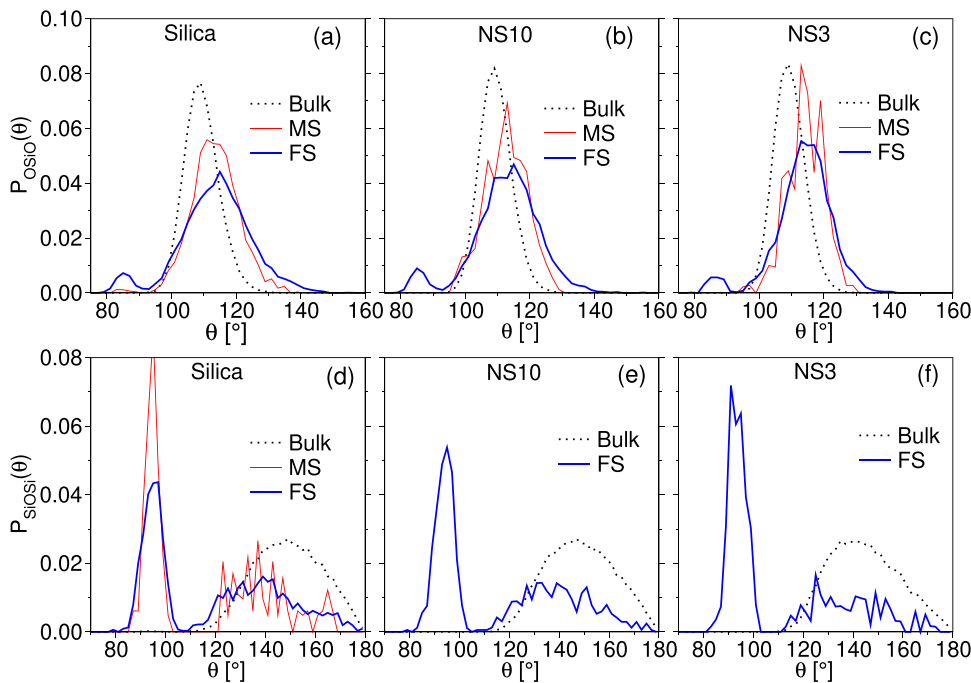


FIG. 9. Bond angle distribution. Panels (a)–(c) are for O–Si–O angles, and panels (d)–(f) for Si–O–Si angles. From left to right, the compositions are silica, NS10, and NS3, respectively.

and NS3, we do not show this distribution for the MS since the quasi-absence of Si atoms makes that the distribution is very noisy.) The abundance of the 2M-rings has also the consequence that the peak found in the bulk system at around 150° , stemming from rings of size 5–7,⁶⁴ is shifted to smaller angles and is reduced significantly in intensity.

Having discussed some of the structural properties of the surfaces for three compositions, we now focus on how the surface composition depends on the Na concentration of the sample. From panel (a) of Fig. 10, one recognizes that for the MS, the Na concentration is significantly higher than the value in the bulk (dashed line), showing that the MS is significantly enriched in sodium. Interestingly, we find that the Na_2O dependence of this concentration closely tracks the one of the bulk (the lines are basically parallel). This means that once the Na_2O concentration of the glass surpasses a certain amount (around 5%), the surface becomes enriched in Na, and increasing the Na_2O concentration does not lead to a modification of the structure beyond the trivially expected amount. For the FS, we find a different behavior in that increasing Na_2O gives rise to a (linear) increase in the Na concentration but this time with a slope that is higher than the one of the bulk. As a consequence, the Na fraction in the FS gradually approaches the one of the MS as the Na_2O concentration is increased. The same qualitative trends are observed for the concentration of oxygen: Both types of surfaces have an O concentration that is higher than the one in the bulk, but now, the one for the MS is closer to the bulk curve than the FS.

Also included in Fig. 10(a) are the experimental data for the FS of NS3 as measured by LEIS,²³ which shows the enrichment of Na in the surface layer, in quantitative agreement with our results. The experimental value for the O concentration is compatible with our

results, but due to the relatively large error bars of the experiment data, one cannot draw strong conclusions.

For the oxygen atoms, one can distinguish between bridging and nonbridging oxygen, and their fractions are depicted in Fig. 10(b). We see that for the bulk glasses, these concentrations show a linear dependence on the Na_2O content and that for all compositions, our data are in excellent agreement with the results of XPS and nuclear magnetic resonance (NMR) studies.^{65–67} We observe that both types of surfaces are more abundant in NBO than the bulk and that this enrichment is more pronounced for the MS. The concentration of NBO on the surface is directly related to the abundance of Na: More Na on the surface results in the breaking of Si–O–Si linkage, thus creating more dangling Si–O[−] bonds, i.e., more NBO.

Figure 10(c) shows the fraction of under-coordinated (3-fold) Si, Si^3 , a typical structural defect on glass surfaces. We note that the concentration of Si^3 is nearly zero for the MS. In contrast to this, the FS has a non-negligible amount of Si^3 and its concentration shows an exponential dependence on Na_2O concentration. The presence of Si^3 on the FS is due to the fact that the glass was fractured at room temperature with a crack velocity on the order of 10^3 m/s, i.e., dynamic fracture.^{50,68} Since at this T , the glass structure is practically frozen, the structural damage caused by the fracture can hardly be healed, leaving some Si atoms under-coordinated. The fact that the fraction of Si^3 depends on the Na concentration demonstrates the crucial role of Na in reducing and repairing the structural damages during fracture.

Using the surface compositions, we have further calculated for the surfaces the per-atom atomic charge Q , which is defined by

$$Q = \sum_{\alpha} f_{\alpha} q_{\alpha}, \quad (3)$$

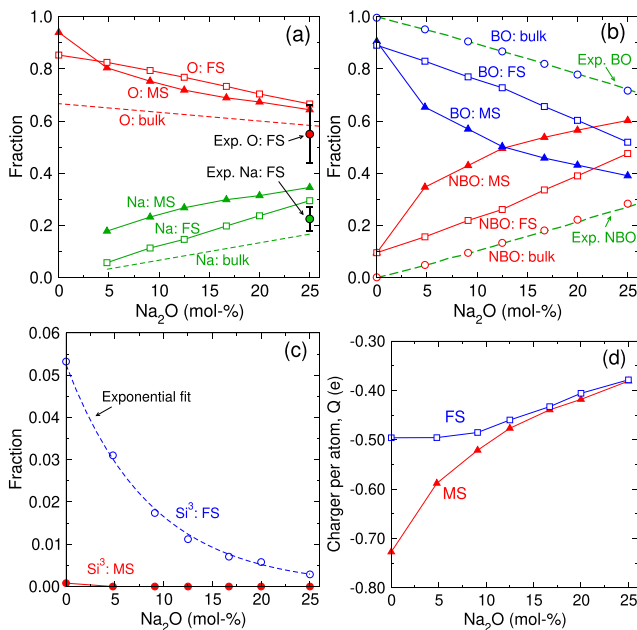


FIG. 10. Surface composition and structure. (a) Fraction of O and Na atoms with respect to the total number of atoms on the surface. Experimental data are taken from Ref. 23. (b) Fraction of BO and NBO species with respect to the total number of O atoms on the surface. The green dashed lines are fits to experimental data, Refs. 65–67. (c) Fraction of undercoordinated Si defects with respect to the total number of Si atoms on the surface. The dashed line is an exponential fit to the FS data. (d) Per-atom atomic charge on the surfaces. Error bars are standard deviation and are smaller than the symbol size for all data points.

where f_α and q_α are the fraction and charge of atom species α ($\alpha \in \{O, Si, Na\}$), respectively. Figure 10(d) shows that both the MS and FS are negatively charged and that the negativity is more pronounced for the MS than for the FS. With increasing Na₂O concentration, $|Q|$ diminishes significantly. These observations are related to the fact that there are more oxygen atoms on the surface than is expected from the stoichiometry, thus giving rise to a local charge imbalance. With increasing Na concentration, sodium atoms will propagate to the surface to compensate the negative charges, rationalizing the decrease in $|Q|$ with increasing Na₂O concentration, although even for the highest concentrations we consider the surface charge remains significantly negative. The charge dependence on the sodium content is stronger for the MS than for the FS since the former is better equilibrated, and hence, the sodium atoms have a higher probability to reach this surface, in agreement with the higher Na fraction found in the MS [Fig. 10(a)].

C. Depth profiles

Having defined the outermost surface layer, we can now investigate how the composition of the sample changes as a function of the depth r , i.e., over what distance the presence of the surface affects the properties of the glass sample. Note that in the following, we define this distance r as the length of the shortest path from a given atom inside the bulk to any atom on the surface, and thus, $r = 0$

represents the surface monolayer. One possible alternative to define a distance for the depth profile would be to use the shortest path between the atom in the glass and an idealized surface. However, since the geometry of such a surface is not known *a priori* (in particular for the FS which is rather rough), additional assumptions would have to be made in the definition of this distance, and in order to avoid such arbitrary choices, we opted for the simple definition of r given above.

Figures 11(a)–11(c) show the concentration profiles of various atomic species as a function of r for the two types of surfaces. These graphs demonstrate that for these three compositions, the curves for the FS and MS are very similar if r exceeds 2 Å–3 Å, while noticeable differences are seen at smaller distances. With increasing r , the oxygen concentration drops very quickly if r reaches 1 Å while the concentration of Si increases strongly. This signals that the atomic layer right below the surface is dominated by silicon atoms, in agreement with the previous studies.^{42,43,63} The distance at which oxygen shows a marked first peak, around 2.3 Å, is not that easy to rationalize since several bonding distances are in this range: O–O of a tetrahedron (2.6 Å), O–O in a 2M ring (2.3 Å), and Na–O (2.25 Å). In addition, the precise position of this peak will depend somewhat on the exact definition of the distance r . As a consequence, we in the following do not discuss the details of this feature. The graph shows that the differences between the curves for the MS and FS become invisible for distances $r > 2$ Å, i.e., beyond this distance, the density profiles do not depend on how the surface has been created. If r is increased further, the elemental concentrations approach the value in the bulk (marked by triangles on the right ordinate), and for distances around 20 Å, the curves reach the bulk values within 1% accuracy. Note that for the systems containing sodium, panels (b) and (c), the decay of the Na profiles is faster than the one for Si and O, a result that is related to the high mobility of the Na atoms, which allows this species to quickly screen the perturbations generated by the surface.

Figures 11(d)–11(f) show the r –dependence of the per-atom atomic charge, defined in Eq. (3), for the two surfaces. As r increases, one finds alternating peaks/valleys, a result that is directly related to the variation of atomic fractions shown in panels [(a)–(c)]. In addition, we notice that the charge fluctuations seem to decay faster if the Na content in the glass is increased. To understand better the r –dependence of Q , we have replotted the data on log–log [Figs. 11(g)–11(i)] and semi-log [Figs. 11(j)–11(l)] scales. (Note that now we plot the absolute value of Q .) These graphs allow to recognize that, within the noise of the data, the charge at intermediate and large distances is independent of the type of surface, despite the fact that the charge on the first layer is more negative for the MS than for the FS, see Fig. 10(d). For the case of silica, panel (g), we find that the decay is nicely described by a power-law with an exponent -2 . If one adds a bit of sodium, NS10 in panel (h), the signal at the intermediate range is compatible with the same power-law, but for distances larger than 8 Å, one spots deviations. For systems with the high sodium content, NS3 in panel (i), the power-law is no longer a good description for the decay.

The log-linear plot in panel (j) confirms that for silica, the decay of $|Q|$ is slower than an exponential. With the addition of Na, NS10 in panel (k), the decay becomes faster, but within the limited r –range of the data, it is not possible to identify the functional form of the decay. However, for the case of NS3, panel (l), things become

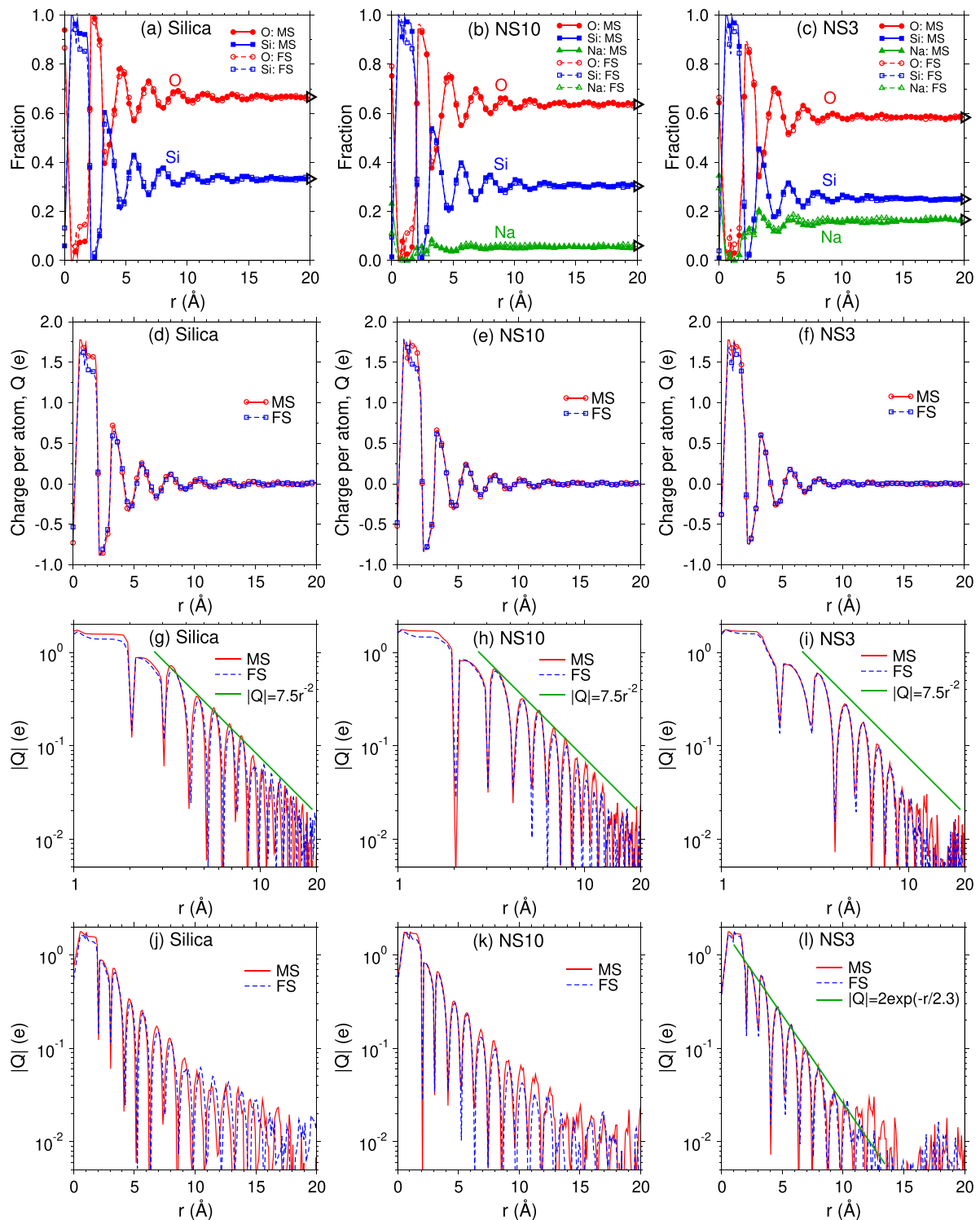


FIG. 11. [(a)–(c)] Depth profiles of elemental concentrations with respect to the monolayer surfaces for silica, NS10, and NS3 (left, middle, right column). In practice, the composition at distance r is the mean over a 1.1 Å thick layer. [(d)–(f)] Depth profiles of the per-atom atomic charge. [(g)–(i)] Log–log plots of the data shown in panels [(d)–(f)]. Note that we now show the absolute value of the atomic charge. The green solid lines in the graphs are guides to the eye and have the slope -2 . [(j)–(l)] Log–linear plots of the data shown in panels [(d)–(f)]. The green solid line in (l) indicates the exponential decay of $|Q|$ with distance r .

clearer in that the signal can be nicely described by a straight line, i.e., the decay is an exponential with a decay length ≈ 2.3 Å. Hence, we can conclude from these graphs that the addition of sodium transforms the power-law decay observed in silica into an exponential decrease, i.e., the network modifier is able to restore the charge balance already at short distances (about 10 Å).

The results in Fig. 11 show that for depths larger than 1 nm–2 nm, the profiles for the FS and MS surfaces are very similar. Thus, we can conclude that the marked differences in the composition and structure between the two types of surfaces, see Figs. 5–10, are washed out very quickly.

Finally, we note that the depth profiles shown in Fig. 11 have some similarities with the partial radial distribution functions $g_{\alpha\beta}(r)$, with $\alpha, \beta \in \{\text{Si}, \text{O}, \text{Na}\}$ [2]. This is related to the fact that the top layer of our surfaces are relatively flat and have a strong asymmetry in their composition, i.e., are abundant in O and Na and depleted in Si. It should be realized, however, that the r -dependence of the depth profile is different from the one of $g_{\alpha\beta}(r)$ since the latter always decays in an exponential manner with increasing r , while we find here power-law like behavior as long as the Na concentration is not too high. So despite the superficial similarities, the two functions are not at all equivalent.

D. Vibrational properties

The quantities discussed so far to characterize the surface are closely related to its structure. In real experiments, it is, however, not easy to access this type of information since, e.g., scattering techniques are hampered by a lack of scattering volume or spatial resolution. As a consequence, one often relies on spectroscopic techniques to investigate surface properties since such measurements allow us to pick up a signal even if the probe volume is small. In order to make a connection of the structural properties with the spectroscopic properties of the samples, we discuss in the present section its vibrational features.

Although simulations using classical potentials have often difficulties to give a reliable description of the vibrational spectra,⁶⁹ the potential used in the present work has been found to be able to reproduce well the vibrational features of soda-silicate glasses in the bulk.^{53,64} Therefore, it can be expected that this potential gives also reasonable values for the vibrational frequencies of the atoms close to the surface.

To calculate the vibrational density of states (VDOS), $g(\omega)$, of the system, we have quenched the glasses to 5 K. Since the samples were already at 300 K, i.e., well below their glass transition temperature, this quench can be done with a high cooling rate without affecting the $g(\omega)$. At this low temperature, the motion of the atoms can be considered to be harmonic, and hence, the VDOS can be obtained by calculating the time Fourier transform of the velocity-autocorrelation function,⁷⁰

$$g(\omega) = \frac{1}{Nk_{\text{B}}T} \sum_j m_j \int_{-\infty}^{\infty} dt \exp(i\omega t) \langle v_j(t) v_j(0) \rangle, \quad (4)$$

where ω is the frequency, N is the number of atoms, k_{B} is the Boltzmann constant, and m_j and $v_j(t)$ are, respectively, the mass and velocity of atom j at time t . This way to calculate $g(\omega)$ has the advantage that it is computationally inexpensive and also allows the

decomposition of the VDOS into various species (atoms, groups of atoms, etc.) by considering on the right-hand side of Eq. (4) the corresponding terms.

Figure 12 shows the frequency dependence of the VDOS, normalized to unity, for three glass compositions. For the case of bulk SiO_2 , dotted line in panel (a), it has been documented that the broad band with $\omega \leq 800 \text{ cm}^{-1}$ is due to bending and rocking modes of O with respect to Si, whereas the high-frequency band with $\omega \geq 950 \text{ cm}^{-1}$ originates from the (symmetric/asymmetric) stretching vibrations within the (SiO_4) units.^{71–73} For the MS, one finds that the high frequency band has the same shape as the one of the bulk, but it is shifted to somewhat lower frequencies, showing that the presence of the surface makes the intra-tetrahedral vibrations a bit softer, likely due to the fact that there are less (effective) constraints on the atoms but also because of the presence of NBO (see below). The bands at around 500 cm^{-1} and 720 cm^{-1} have a lower intensity than the ones in the bulk, and below, we will see that this is due to the increased number of NBO.⁷⁴ This enhanced concentration of NBO is also the reason for the increase in the peak at around 100 cm^{-1} since in this frequency range, one has significant contributions from the rotation of (SiO_4) units.⁷³ For the FS, we see that the gap in $g(\omega)$ at around 850 cm^{-1} starts to fill up since, see below, in this range of ω , the edge sharing BO have a significant contribution to $g(\omega)$. The band at high frequencies has less structure than the one for the bulk or the MS, a result that is related to the increased disorder in the tetrahedral units. The rest of the spectrum is qualitatively similar to the one for the MS, except that the peak at around 100 cm^{-1} is shifted to even lower frequencies since the structural units at the surface have a decreased connectivity.

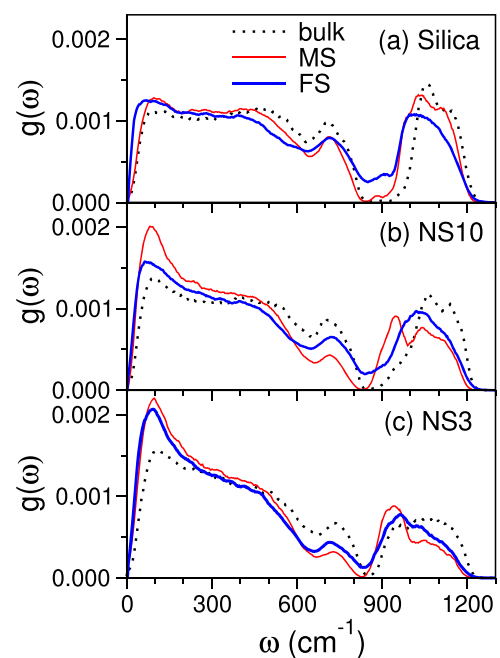


FIG. 12. Total vibrational density of states at 5 K. [(a)–(c)] are for silica, NS10, and NS3 glasses, respectively. All VDOS curves are normalized to unity.

For the bulk glasses containing Na, Figs. 12(b) and 12(c), we note firstly that the intensities of the main bands at intermediate and high frequencies are reduced with respect to the ones in silica. In contrast to this, one observes the presence of a pronounced peak at $\omega < 200 \text{ cm}^{-1}$, the intensity of which increases with increasing Na concentration. This peak is related to the vibrational modes of the Na atoms.⁷⁵ For the surfaces, this low-frequency peak is significantly higher than the one of the bulk, in agreement with the fact discussed above that the surfaces have higher concentration of Na and NBO (Fig. 10). The increase in Na content also leads to a substantial reduction of the peak at around 720 cm^{-1} since the presence of Na reduces the number of corner-sharing bridging oxygen atoms (see below). For the high frequency band, we recognize that the presence of a surface leads to a significant change in the shape of the peaks, excitations that are related to complex Si-O and Si-NBO motions.^{74,75}

In order to understand in a more quantitative manner the reason for these modifications, it is useful to decompose the VDOS into the contributions of the various structural elements. Figures 13(a) and 13(b) present the various partial VDOS for the FS of the silica glass. The structural elements we consider are the edge-sharing and corner-sharing BO (esBO and csBO, respectively), the edge-sharing and corner-sharing silicon atoms (esSi and csSi, respectively) as well as the NBO. [For the sake of clarity, these five partials are shown separately in panels (a) and (b).] Also included in the graphs are the total VDOS (the same as shown in Fig. 12, but here it is normalized with respect to the number of atoms). The total VDOS is the weighted sum of the partials, with weights that are stated next to each curve. From these distributions, one recognizes that around 950 cm^{-1} , the NBO as well as the esBO have a sharp peak. This rationalizes thus the observation that in Fig. 12(a), the high frequency band of the FS is shifted to lower frequency with respect to the bulk system. The disappearance of the gap at around 850 cm^{-1} can now be explained by a signal in the VDOS of the esBO since these 2M-rings have a marked

peak at $\approx 880 \text{ cm}^{-1}$ [panel (a)]. We mention that the experimental studies have reported that the presence of 2M-rings on the surface of β -cristobalite and amorphous silica gives rise to two strong infrared bands at 888 cm^{-1} and 908 cm^{-1} and a shoulder at 932 cm^{-1} .^{30,32,35,36} The vibrational fingerprint of 2M-ring found in our simulations is thus in excellent agreement with these experimental findings. To the best of our knowledge, this is the first time the vibrational signature of the 2M-ring structure is correctly predicted from classical simulations.

Furthermore, we note that the 2M-rings affect also the total spectrum at lower frequencies. The spectrum for the csBO has a peak at around 420 cm^{-1} [Fig. 13(b)], while for the esBO, this peak is shifted to around 300 cm^{-1} , which rationalizes the different shape of the total VDOS in this frequency range [see Fig. 12(a)]. Panel (b) also shows that the NBO have a marked peak at around 80 cm^{-1} . This feature explains thus why the total VDOS for the FS has an enhanced intensity at low frequencies with respect to the bulk sample.

We show in Figs. 13(c) and 13(d) the partial VDOS for the MS and FS of the Na-containing NS3 glass. For both systems, we find that the Na VDOS has a pronounced peak at small frequencies, in qualitative agreement with the previous simulation results of bulk systems.⁷⁵ Note that for the FS, this peak is somewhat higher than the one for the MS. This is likely due to the fact that for the MS, the local Na concentration is higher than for the FS, thus allowing environments of the Na atoms that are more diverse and hence a peak that is broader. Furthermore, we see that the curves for the NBO have a pronounced peak at $\approx 950 \text{ cm}^{-1}$, while the one for BO have a strong contribution at $\omega > 1000 \text{ cm}^{-1}$. These two peaks explain thus the observed double peak structure in NS3 in the high frequency band of the NS3 system having a surface, see Fig. 12(c).

Finally, we note that for the FS, we can also detect a small peak at $\omega \approx 860 \text{ cm}^{-1}$ in the VDOS for the Si and BO, panel (d), while this feature is absent in the spectra for the MS. These peaks are related to

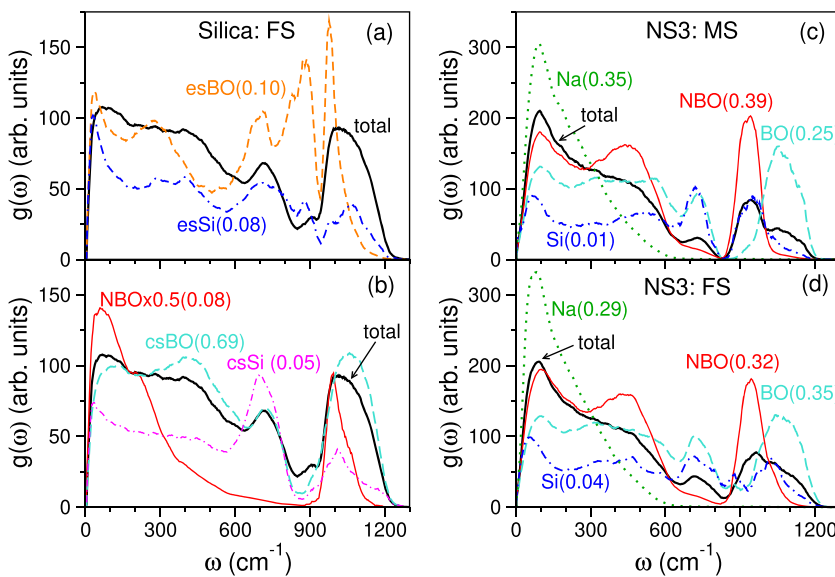


FIG. 13. Per-atom VDOS of various atomic species. The number in the parenthesis is the fraction of a given species with respect to the total. (a) and (b) are for the FS of silica. The curve for NBO is multiplied by 0.5 to allow better comparison. (c) and (d) are for the MS and FS of NS3, respectively.

the 2M-rings of the surface, which are present on the FS but not on the MS (see Fig. 7). So this peak is able to tell whether a surface has been generated from a quench of the melt or the fracture of a glass sample.

IV. SUMMARY AND CONCLUSIONS

In this work, we have probed how the properties of glass surfaces depend on the composition of the system and the type of surface considered (melt-formed surface or fracture surface). By analyzing the surface monolayer, we have found that, independent of the Na₂O concentration, there are significant differences between the MS and FS; the latter have quite a few structural defects such as two-membered rings and under-coordinated Si, while the former have none, except for the case of silica. This shows that for the MS, the annealing of the structure as made possible by the high-temperature equilibration and slow cooling allows us to avoid these energetically unfavorable structures, if Na are present. The composition of the first atomic layer also depends on the type of sample considered in that the elemental concentrations of the FS show almost a linear dependence on the Na₂O content in the glass, whereas the ones for the MS behave very differently. Both the MS and FS are negatively charged. For the glasses with low Na₂O concentration, this charge is relatively large but its negativity decreases with increasing Na₂O content. This effect can be expected to be important for the chemical reactivity of the surface since local Na fluctuations will result in local fluctuations in the charge.

Since the presence of the surface creates a gradient in the composition, we have probed how these fluctuations depend on the type of surface and the glass composition. Surprisingly, we find that beyond the second atomic layer below the surface, i.e., $r > 2 \text{ \AA}$, there is no noticeable difference between the compositional fluctuations measured in the FS and MS systems. We emphasize, however, that this result does not mean that the structure of the glass farther than, say, a few Å from the surface is independent of the way the surface was generated. Interestingly, the functional form for the decay of the elemental concentration depends on the Na₂O concentration in the sample: For low Na₂O concentration, it is a power-law, while for high concentration one finds an exponential decay. The slower (power-law) decay indicates the high local frustration of the system, which permits only a gradual healing of the structural perturbation due to the presence of free surface.

The vibrational density of states show that the systems with free surfaces have on average atomic vibrations at lower frequencies than the one found in the bulk glass. By analyzing the partial VDOS, we show that this softening of the atomic vibrations is due to the increased number of NBO close to the surface and also to the higher concentration of Na atoms. Interestingly, we find in the spectrum of the FS a weak but clear signal of the two-membered rings at the frequency of $\approx 880 \text{ cm}^{-1}$, while no such signal exists for the MS. This result therefore permits one to use spectroscopic methods to decide whether or not a given surface has been generated from a fracture process.

ACKNOWLEDGMENTS

We thank H. Jain for discussions. Z.Z. acknowledges financial support by China Scholarship Council (Grant No. 201606050112).

W.K. is member of the Institut Universitaire de France. This work was granted access to the HPC resources of CINES under the allocations (Grant Nos. A0050907572 and A0070907572) attributed by GENCI (Grand Equipement National de Calcul Intensif).

DATA AVAILABILITY

The data that support the findings of this study are available from the corresponding author upon reasonable request.

REFERENCES

- 1 J. E. Shelby, *Introduction to Glass Science and Technology* (Royal Society of Chemistry, 2005).
- 2 K. Binder and W. Kob, *Glassy Materials and Disordered Solids: An Introduction to Their Statistical Mechanics* (World Scientific, 2011).
- 3 A. K. Varshneya, *Fundamentals of Inorganic Glasses* (Elsevier, 2013).
- 4 L. L. Hench and D. E. Clark, "Physical chemistry of glass surfaces," *J. Non-Cryst. Solids* **28**(1), 83–105 (1978).
- 5 C. G. Pantano, "Glass surfaces," *Rev. Solid State Sci.* **3**, 379–408 (1989).
- 6 H. Bach, "Advanced surface analysis of silicate glasses, oxides and other insulating materials: A review," *J. Non-Cryst. Solids* **209**(1–2), 1–18 (1997).
- 7 P. L. Bocko, P. M. Fenn, L. R. Morse, and F. Okamoto, "Surface chemistry and microstructure of flat panel display substrates," in *SID 91 Digest* (Society for Information Display, 1991), Vol. 675.
- 8 T. Dey and D. Naughton, "Cleaning and anti-reflective (Ar) hydrophobic coating of glass surface: A review from materials science perspective," *J. Sol-Gel Sci. Technol.* **77**(1), 1–27 (2016).
- 9 K. Zheng, M. Kapp, and A. R. Boccaccini, "Protein interactions with bioactive glass surfaces: A review," *Appl. Mater. Today* **15**, 350–371 (2019).
- 10 T. L. Anderson, *Fracture Mechanics: Fundamentals and Applications*, 4th ed. (CRC Press, 2017).
- 11 M. A. Meyers and K. K. Chawla, *Mechanical Behavior of Materials* (Cambridge University Press, 2008).
- 12 M. Ciccotti, "Stress-corrosion mechanisms in silicate glasses," *J. Phys. D: Appl. Phys.* **42**(21), 214006 (2009).
- 13 C. L. Rountree, S. Prades, D. Bonamy, E. Bouchaud, R. Kalia, and C. Guillot, "A unified study of crack propagation in amorphous silica: Using experiments and simulations," *J. Alloys Compd.* **434–435**, 60–63 (2007).
- 14 P. K. Gupta, D. Inniss, C. R. Kurkjian, and Q. Zhong, "Nanoscale roughness of oxide glass surfaces," *J. Non-Cryst. Solids* **262**(1–3), 200–206 (2000).
- 15 T. Sarlat, A. Lelarge, E. Søndergård, and D. Vandembroucq, "Frozen capillary waves on glass surfaces: An AFM study," *Eur. Phys. J. B* **54**(1), 121–126 (2006).
- 16 D. Bonamy, L. Ponson, S. Prades, E. Bouchaud, and C. Guillot, "Scaling exponents for fracture surfaces in homogeneous glass and glassy ceramics," *Phys. Rev. Lett.* **97**(13), 135504 (2006).
- 17 L. Ponson, D. Bonamy, and E. Bouchaud, "Two-dimensional scaling properties of experimental fracture surfaces," *Phys. Rev. Lett.* **96**(3), 035506 (2006).
- 18 S. M. Wiederhorn, J. M. López-Cepero, J. Wallace, J.-P. Guin, and T. Fett, "Roughness of glass surfaces formed by sub-critical crack growth," *J. Non-Cryst. Solids* **353**(16–17), 1582–1591 (2007).
- 19 J.-P. Guin and S. Wiederhorn, "Fracture of silicate glasses: Ductile or brittle?," *Phys. Rev. Lett.* **92**(21), 215502 (2004).
- 20 D. Bonamy and E. Bouchaud, "Failure of heterogeneous materials: A dynamic phase transition?," *Phys. Rep.* **498**(1), 1–44 (2011).
- 21 S. M. Wiederhorn, T. Fett, J.-P. Guin, and M. Ciccotti, "Griffith cracks at the nanoscale," *Int. J. Appl. Glass Sci.* **4**(2), 76–86 (2013).
- 22 J. F. Kelso, C. G. Pantano, and S. H. Garofalini, "A comparison of ion scattering spectra and molecular dynamics simulations at the surface of silicate glasses," *Surf. Sci. Lett.* **134**(3), L543–L549 (1983).

- ²³R. M. Almeida, R. Hickey, H. Jain, and C. G. Pantano, "Low-energy ion scattering spectroscopy of silicate glass surfaces," *J. Non-Cryst. Solids* **385**, 124–128 (2014).
- ²⁴R. M. Almeida, H. Jain, and C. G. Pantano, "Low-energy ion-scattering spectroscopy of modified silicate glasses," *J. Am. Ceram. Soc.* **99**(4), 1259–1265 (2016).
- ²⁵C. V. Cushman, P. Brüner, J. Zakel, C. Dahlquist, B. Sturgell, T. Grehl, B. M. Lunt, J. Banerjee, N. J. Smith, and M. R. Linford, "Low energy ion scattering (LEIS) of as-formed and chemically modified display glass and peak-fitting of the Al/Si LEIS peak envelope," *Appl. Surf. Sci.* **455**, 18–31 (2018).
- ²⁶E. Rädlein and G. H. Frischat, "Atomic force microscopy as a tool to correlate nanostructure to properties of glasses," *J. Non-Cryst. Solids* **222**, 69–82 (1997).
- ²⁷J.-F. Poggemann, A. Goss, G. Heide, E. Rädlein, and G. H. Frischat, "Direct view of the structure of a silica glass fracture surface," *J. Non-Cryst. Solids* **281**(1-3), 221–226 (2001).
- ²⁸J.-F. Poggemann, G. Heide, and G. H. Frischat, "Direct view of the structure of different glass fracture surfaces by atomic force microscopy," *J. Non-Cryst. Solids* **326**, 15–20 (2003).
- ²⁹G. H. Frischat, J.-F. Poggemann, and G. Heide, "Nanostructure and atomic structure of glass seen by atomic force microscopy," *J. Non-Cryst. Solids* **345**, 197–202 (2004).
- ³⁰B. A. Morrow and I. A. Cody, "Infrared studies of reactions on oxide surfaces. 5. Lewis acid sites on dehydroxylated silica," *J. Phys. Chem.* **80**(18), 1995–1998 (1976).
- ³¹T. A. Michalske and B. C. Bunker, "Slow fracture model based on strained silicate structures," *J. Appl. Phys.* **56**(10), 2686–2693 (1984).
- ³²B. C. Bunker, D. M. Haaland, K. J. Ward, T. A. Michalske, W. L. Smith, J. S. Binkley, C. F. Melius, and C. A. Balfe, "Infrared spectra of edge-shared silicate tetrahedra," *Surf. Sci.* **210**(3), 406–428 (1989).
- ³³L. H. Dubois and B. R. Zegarski, "Bonding of alkoxy silanes to dehydroxylated silica surfaces: A new adhesion mechanism," *J. Phys. Chem.* **97**(8), 1665–1670 (1993).
- ³⁴L. H. Dubois and B. R. Zegarski, "Reaction of alkoxy silane coupling agents with dehydroxylated silica surfaces," *J. Am. Chem. Soc.* **115**(3), 1190–1191 (1993).
- ³⁵A. Grabbe, T. A. Michalske, and W. L. Smith, "Strained siloxane rings on the surface on silica: Their reaction with organosiloxanes, organosilanes, and water," *J. Phys. Chem.* **99**(13), 4648–4654 (1995).
- ³⁶A. M. Ferrari, E. Garrone, G. Spoto, P. Ugliengo, and A. Zecchina, "Reactions of silica strained rings: An experimental and *ab-initio* study," *Surf. Sci.* **323**, 151 (1995).
- ³⁷A. Rimola, D. Costa, M. Sodupe, J.-F. Lambert, and P. Ugliengo, "Silica surface features and their role in the adsorption of biomolecules: Computational modeling and experiments," *Chem. Rev.* **113**(6), 4216–4313 (2013).
- ³⁸M. Ren, L. Deng, and J. Du, "Bulk, surface structures and properties of sodium borosilicate and boroaluminosilicate nuclear waste glasses from molecular dynamics simulations," *J. Non-Cryst. Solids* **476**, 87–94 (2017).
- ³⁹T. S. Mahadevan and J. Du, "Hydration and reaction mechanisms on sodium silicate glass surfaces from molecular dynamics simulations with reactive force fields," *J. Am. Ceram. Soc.* **103**(6), 3676–3690 (2020).
- ⁴⁰B. P. Feuston and S. H. Garofalini, "Topological and bonding defects in vitreous silica surfaces," *J. Chem. Phys.* **91**(1), 564–570 (1989).
- ⁴¹S. H. Garofalini, "Molecular dynamics computer simulations of silica surface structure and adsorption of water molecules," *J. Non-Cryst. Solids* **120**(1-3), 1–12 (1990).
- ⁴²A. Roder, W. Kob, and K. Binder, "Structure and dynamics of amorphous silica surfaces," *J. Chem. Phys.* **114**(17), 7602–7614 (2001).
- ⁴³M. Rarivomanantsoa, P. Jund, and R. Jullien, "Classical molecular dynamics simulations of amorphous silica surfaces," *J. Phys.: Condens. Matter* **13**(31), 6707 (2001).
- ⁴⁴J. Du and A. N. Cormack, "Molecular dynamics simulation of the structure and hydroxylation of silica glass surfaces," *J. Am. Ceram. Soc.* **88**(9), 2532–2539 (2005).
- ⁴⁵D. Ceresoli, M. Bernasconi, S. Iarlori, M. Parrinello, and E. Tosatti, "Two-membered silicon rings on the dehydroxylated surface of silica," *Phys. Rev. Lett.* **84**(17), 3887 (2000).
- ⁴⁶N. P. Bansal and R. H. Doremus, *Handbook of Glass Properties* (Academic Press, Orlando, 1986).
- ⁴⁷A. Fluegel, "Global model for calculating room-temperature glass density from the composition," *J. Am. Ceram. Soc.* **90**(8), 2622–2625 (2007).
- ⁴⁸R. Knoche, D. B. Dingwell, F. A. Seifert, and S. L. Webb, "Non-linear properties of supercooled liquids in the system Na₂O–SiO₂," *Chem. Geol.* **116**(1-2), 1–16 (1994).
- ⁴⁹P. Richet and Y. Bottinga, "Glass transitions and thermodynamic properties of amorphous SiO₂, NaAlSi_nO_{2n+2} and KAlSi₃O₈," *Geochim. Cosmochim. Acta* **48**(3), 453–470 (1984).
- ⁵⁰Z. Zhang, "Fracture, surface, and structure of silicate glasses: Insights from atomistic computer simulations," Ph.D. dissertation (University of Montpellier, 2020), <https://hal.archives-ouvertes.fr/tel-02902601>.
- ⁵¹Z. Zhang, S. Ispas, and W. Kob, "The critical role of the interaction potential and simulation protocol for the structural and mechanical properties of sodosilicate glasses," *J. Non-Cryst. Solids* **532**, 119895 (2020).
- ⁵²A. Pedone, G. Malavasi, M. C. Menziani, U. Segre, and A. N. Cormack, "Molecular dynamics studies of stress-strain behavior of silica glass under a tensile load," *Chem. Mater.* **20**(13), 4356–4366 (2008).
- ⁵³S. Sundararaman, L. Huang, S. Ispas, and W. Kob, "New optimization scheme to obtain interaction potentials for oxide glasses," *J. Chem. Phys.* **148**(19), 194504 (2018).
- ⁵⁴S. Nosé, "A unified formulation of the constant temperature molecular dynamics methods," *J. Chem. Phys.* **81**(1), 511–519 (1984).
- ⁵⁵W. G. Hoover, "Canonical dynamics: Equilibrium phase-space distributions," *Phys. Rev. A* **31**(3), 1695–1697 (1985).
- ⁵⁶W. G. Hoover, "Constant-pressure equations of motion," *Phys. Rev. A* **34**(3), 2499–2500 (1986).
- ⁵⁷S. Plimpton, "Fast parallel algorithms for short-range molecular dynamics," *J. Comput. Phys.* **117**(1), 1–19 (1995).
- ⁵⁸H. Edelsbrunner and E. P. Mücke, "Three-dimensional alpha shapes," *ACM Trans. Graphics* **13**(1), 43–72 (1994).
- ⁵⁹A. Stukowski, "Computational analysis methods in atomistic modeling of crystals," *JOM* **66**(3), 399–407 (2014).
- ⁶⁰A. Stukowski, "Visualization and analysis of atomistic simulation data with OVITO—the Open Visualization Tool," *Modell. Simul. Mater. Sci. Eng.* **18**(1), 015012 (2010).
- ⁶¹J. F. Kelso and C. G. Pantano, "Spectroscopic examination of clean glass surfaces at elevated temperatures," *J. Vac. Sci. Technol.* **3**(3), 1343–1346 (1985).
- ⁶²C. Mischler, W. Kob, and K. Binder, "Classical and *ab-initio* molecular dynamic simulation of an amorphous silica surface," *Comput. Phys. Commun.* **147**(1-2), 222–225 (2002).
- ⁶³S. Halbert, S. Ispas, C. Raynaud, and O. Eisenstein, "Modelling the surface of amorphous dehydroxylated silica: The influence of the potential on the nature and density of defects," *New J. Chem.* **42**(2), 1356–1367 (2018).
- ⁶⁴S. Sundararaman, L. Huang, S. Ispas, and W. Kob, "New interaction potentials for alkali and alkaline-earth aluminosilicate glasses," *J. Chem. Phys.* **150**(15), 154505 (2019).
- ⁶⁵B. W. Veal, D. J. Lam, A. P. Paulikas, and W. Y. Ching, "XPS study of CaO in sodium silicate glass," *J. Non-Cryst. Solids* **49**(1-3), 309–320 (1982).
- ⁶⁶H. Maekawa, T. Maekawa, K. Kawamura, and T. Yokokawa, "The structural groups of alkali silicate glasses determined from ²⁹Si MAS-NMR," *J. Non-Cryst. Solids* **127**(1), 53–64 (1991).
- ⁶⁷H. W. Nesbitt, G. M. Bancroft, G. S. Henderson, R. Ho, K. N. Dalby, Y. Huang, and Z. Yan, "Bridging, non-bridging and free (O²⁻) oxygen in Na₂O–SiO₂ glasses: An x-ray Photoelectron Spectroscopic (XPS) and Nuclear Magnetic Resonance (NMR) study," *J. Non-Cryst. Solids* **357**(1), 170–180 (2011).
- ⁶⁸G. D. Quinn, "On terminal crack velocities in glasses," *Int. J. Appl. Glass Sci.* **10**(1), 7–16 (2019).
- ⁶⁹M. Benoit and W. Kob, "The vibrational dynamics of vitreous silica: Classical force fields vs first principles," *Europhys. Lett.* **60**(2), 269 (2002).

⁷⁰M. T. Dove, *Introduction to Lattice Dynamics* (Cambridge University Press, 1993).

⁷¹M. Wilson, P. A. Madden, M. Hemmati, and C. A. Angell, "Polarization effects, network dynamics, and the infrared spectrum of amorphous SiO₂," *Phys. Rev. Lett.* **77**(19), 4023 (1996).

⁷²J. Sarnthein, A. Pasquarello, and R. Car, "Origin of the high-frequency doublet in the vibrational spectrum of vitreous SiO₂," *Science* **275**(5308), 1925–1927 (1997).

⁷³S. N. Taraskin and S. R. Elliott, "Nature of vibrational excitations in vitreous silica," *Phys. Rev. B* **56**(14), 8605–8622 (1997).

⁷⁴N. Zotov, I. Ebbsjö, D. Timpel, and H. Keppler, "Calculation of Raman spectra and vibrational properties of silicate glasses: Comparison between Na₂Si₄O₉ and SiO₂ glasses," *Phys. Rev. B* **60**(9), 6383–6397 (1999).

⁷⁵D. Kilymis, S. Ispas, B. Hehlen, S. Peuket, and J.-M. Delaye, "Vibrational properties of sodosilicate glasses from first-principles calculations," *Phys. Rev. B* **99**(5), 054209 (2019).